Efficient catalytic ozonation over Co-ZFO@Mn-CN for oxalic acid degradation: Synergistic effect of oxygen vacancies and HOO-Mn-N$_X$ bonds

Menglu Xu [a],[1], Yibing Zhang [a],[1], Huaqin Yin [a], Jinnan Wang [a],[*], Aimin Li [a], Philippe François-Xavier Corvini [b]

[a] *State Key Laboratory of PolS2lution Control and Resource Reuse & School of the Environment Nanjing University, Nanjing 210023, China*
[b] *School of Life Sciences, University of Applied Sciences and Arts Northwestern Switzerland, Basel 4132, Switzerland*

A B S T R A C T

Co-ZFO@Mn-CN with $^1O_2$ and $O_2^{\bullet-}$ as main reactive oxygen species was synthesized for catalytic ozonation, which could efficiently degrade organic pollutants. EPR and XPS analysis indicated that lattice doping of Co induced formation of abundant of OVs, which could provide localized electrons for O_3 activation with the generation of $HO_2^{\bullet}/O_2^{\bullet-}$. $^1O_2$ and H_2O_2 were produced by the recombination of $HO_2^{\bullet}/O_2^{\bullet-}$. DFT calculation demonstrated that H_2O_2 was deprotonated to generate HOO^-, which preferred to form HOO-Mn-N$_X$ bonds with Co-ZFO@Mn-CN. Under the attack of O_3, HOO-Mn-N$_X$ bonds were broken with the generation of $HO_2^{\bullet}$ and $HO_3^{\bullet}/O_3^{\bullet-}$, not only accelerating $^1O_2$ production for organics degradation but also avoiding Mn(II) sites oxidation. Combining advantages of OVs and HOO-Mn-N$_X$, Co-ZFO@Mn-CN achieved 70–100% mineralization for different organic pollutants. Thus, this work provided a simple and efficient way for enhancing the utilization of O_3 by the synergistic effect of OVs and HOO-Mn-N$_X$ bonds, also improving ROS transformation.

1. Introduction

Advanced oxidation processes (AOPs) are widely used for refractory organic pollutants degradation, such as ozonation, Fenton/Fenton-like reaction [1–9], electrochemically oxidation [10–14], and photo-catalytic oxidation [15–22]. As a highly efficient and eco-friendly technique without chemical residues, ozonation arose much attention especially in the field of wastewater treatment [23–25]. For a heterogeneous reaction system, ozonation process could be improved by reducing bubbles size or optimizing the reactors involving the acceleration of ozone gas-liquid mass transfer [26]. By contrast, catalyzing ozone conversion into radicals could enhance the organics degradation more efficiently because interface interaction between substrates and catalysts not only promoted the reactive oxygen species (ROS) generation but also facilitated the organic pollutants enrichment on active sites [27–31].

On the other hand, as an electrophilic agent, O_3 preferred to attack the unsaturated bonds (such as alkene π-bond) of organic compounds with production of large amounts of intermediates [32,33]. These intermediates accumulated in ozonation reaction system inevitably

competed with substrates, seriously inhibiting the mineralization of organics. Different from O_3 selectively attacking unsaturated bonds, non-selective oxidation process caused by $^{\bullet}OH$ and $O_2^{\bullet-}$ usually achieved much higher mineralization efficiency. Unfortunately, without catalysts, spontaneous decomposition kinetics of O_3 into $^{\bullet}OH$ and $O_2^{\bullet-}$ is extremely slow at room temperature under atmospheric pressure [34–36]. Previous studies demonstrated that metal-O bonds constructed could facilitate the electrons transferred from transition metal to O_3 for generation of radicals [37–39]. Owing to multiple valence state transformation, MnO_X [40–44] and CeO_2 [45–48] were commonly used to catalyze ozonation involving the redox reactions between transition metal and O_3 ($\equiv Mn^{3+}-OH + O_3 \rightarrow Mn^{4+} + O_L + HO_3^{\bullet}$, $\equiv Ce^{3+}-2OH_2^+ + 4\,O_3 \rightarrow \equiv Ce^{4+} + 2\,O^{2-} + 4HO_3^{\bullet}$). However, due to different kinetic constants between reduction and oxidation reactions [49], oxidation state transition metal would be accumulated seriously with the catalytic ozonation proceeding, resulting in catalysts inactivation and transition metal leaching out.

Notably, the lattice doping of different transition metals could induce the formation of OVs [50], and O_3 preferred to be adsorbed on OVs for conversion into $HO_2^{\bullet}/O_2^{\bullet-}$ and $^1O_2$ [51]. Spontaneous recombination of

---

* Corresponding author.
  E-mail address: wjnnju@163.com (J. Wang).
  [1] First author: Menglu Xu and Yibing Zhang contributed equally to this work.

$HO_2^{\bullet}$ would occur with the generation of H_2O_2 and $^1O_2$ ($2\,HO_2^{\bullet} \rightarrow H_2O_2 + \,^1O_2$) [52], significantly enhancing the utilization of oxidants (ROS) for organics degradation. Previous work demonstrated that bi-metallic catalyst might provide the supporting ligand in the interface of ozone-H_2O_2-catalysts and metal-H_2O_2 complexes which could be decomposed into $HO_2^{\bullet}$ under the attack of O_3. Owing to its rich OVs, Co doping $ZnFe_2O_4$ (Co-ZFO) was reported for PMS activation [53,54], where OVs not only provided active site for PMS adsorption but also acted as a medium for the electrons transport from organics to PMS. On the other hand, transition metal-coordinated nitrogen-carbon materials (M-N-C) developed for oxygen reduction reaction (ORR) could promote the charge transport because the increased local density of states (DOS) around the Fermi level by the formation of Mn-N coordination could enhance charge migration. More importantly, oxidants such as H_2O_2 adsorbed at transition metal-coordinated nitrogen bonds could form the HOO-M-N species which preferred to be broken, accompanying with transition metal reduction [55,56]. Thus, it is expected to resolve the problem of the transition metal deactivation during the catalytic ozonation by combining Mn-N-C with Co-ZFO.

Based on the above research background and conception, novel catalyst Co-ZFO@Mn-CN with abundant of OVs and Mn-CN sites was synthesized for O_3 activation, which could efficiently degrade organic pollutants. Different from traditional catalytic ozonation mechanism involving classic Fenton-like reaction, OVs in Co-ZFO@Mn-CN could provide abundant localized electrons for O_3 activation with the generation of large amounts of $HO_2^{\bullet}/O_2^{\bullet-}$. Subsequently, H_2O_2 was produced from the recombination of $HO_2^{\bullet}/O_2^{\bullet-}$. As the deprotonation product of H_2O_2, HOO^- could form HOO-Mn-N_X bonds with Co-ZFO@Mn-CN which preferred to be attacked by O_3 with the generation of $HO_2^{\bullet}$ and $HO_3^{\bullet}/O_3^{\bullet-}$, avoiding the catalyst deactivation caused by Mn(II) oxidation. Thus, both O_3 utilization and catalyst stability were significantly improved.

2. Experiment

2.1. Chemicals and materials

Zinc acetate dihydrate (99.0%), Cobalt acetate tetrahydrate (99.5%), Citric acid monohydrate (99.5%), Manganese(II) chloride tetrahydrate (99.0%), Tert-Butyl alcohol (t-BA, 99.0%), Sodium azide (NaN$_3$ 99.0%) and Nitricacid (HNO$_3$, 68%) were obtained from Nanjing Chemical Reagent Co. Ltd. Dicyandiamide (99.0%), Oxalic acid (OA, 99.0%), Para-benzoquinone (p-BQ, 99.5%), Rhodamine B (RhB), Bisphenol A (BPA), p-hydroxylbenzoic acid (PHBA), 1 H-Benzotriazole (BZA), 2,4-Dichlorophenoxyacetic acid (2,4-D) were purchased from Aladdin Co. Ltd. China. Iron(III) nitrate nonahydrate (98.5%) was supplied by Shanghai Macklin Biochemical Co. Ltd. China. 5,5-Dimethyl-1-pyrroline N-oxide (DMPO, 98.0%) was obtained from Sigma-Aldrich Co. Ltd. 2,2,6,6-Tetramethylpiperidine (TEMP, 98.0%) was purchased from Tokyo Chemical Industry Co. Ltd. Milli-Q water (18.2 MΩ·cm in resistivity, Millipore) was used throughout the experiments. All chemicals and reagents were used without further purification.

2.2. Preparation of Co-ZFO@Mn-CN

The synthesis process of Co-ZFO@Mn-CN is shown in Scheme S1.

2.2.1. Preparation of Co-ZFO

Typically, Co-ZFO was synthesized using the sol-gel method. Zn (CH$_3$COO)$_2$0.2 H$_2$O (5.0 mmol), Fe(NO$_3$)$_3$0.9 H$_2$O (7.0 mmol), Co (CH$_3$COO)$_2$0.4 H$_2$O (3.0 mmol) and 30.0 mmol citric acid monohydrate were dissolved in the diluted nitric acid solution with stirring (200 rpm) for 30 min. Then the mixture was kept in water-bath heating at 90 °C for 3 h to obtain the viscous gel. After heated at 170 °C (heating rate of 10 °C/min) for 12 h and subsequently calcined at 600 °C (heating rate of 5 °C/min) for 6 h, black powder (Co-ZFO) was obtained.

2.2.2. Preparation of Co-ZFO@Mn-CN

1.0 g dicyandiamide and 0.12 g MnCl$_2$0.4 H$_2$O were dissolved in 20 mL deionized water at 70 ℃ under stirring (200 rpm). Then, 11 mg Co-ZFO was dispersed in the solution and the mixture was heated at 80 ℃ for 12 h in a vacuum drying over. The obtained power was heated at 600 ℃ (heating rate of 10 ℃/min) for 3 h in a tubular furnace under nitrogen atmosphere. Finally, catalyst Co-ZFO@Mn-CN was obtained.

2.3. Characterization methods

The surface morphology and elemental composition of catalysts were analyzed by a scanning electron microscope (SEM, ZEISS Supra 55, Germany). Besides, high resolution transmission electron microscopy (HR-TEM, JEOL, JEM-2100 f, Japan) with 200 kV electron beam accelerating voltage was used to determine the lattice spacing of the catalysts. The crystal structure of the catalysts was characterized by X-ray diffraction (XRD, Bruker, Germany) with a Cu Kα irradiation over the 2θ range of 10–80°. The surface functional groups were exhibited by Fourier transform infrared spectra (FT-IR, Thermo Scientific Nicolet iS20, America). Surface chemical valence states of catalysts were analyzed using the X-ray photoelectron spectrum (XPS, ULVAC-PHI, Japan). All binding energies of XPS curves were referenced to the C 1 s peak at 284.8 eV as XPS curves during the deconvolution process. Electron paramagnetic resonance (EPR) spectra of the catalysts were obtained using an electron paramagnetic resonance spectrometer (Bruker model EMXplus-6/1), which could confirm the existence of OVs on catalyst surface. To identify the ROS in reaction system, oxalic acid was replaced by DMPO or TEMP as ROS trapping agent, with the measuring condition at 20 °C and 5 min of reaction (microwave frequency 9.824 GHz, sweep width 100 G, sweep time 30.00 s, modulation frequency 100 kHz, modulation width 1 G, microwave power 6.325 mW).

To identify the reactive species in reaction system, chronoamperometry curves (CA) was measured by the electrochemical workstation (CHI660E, Shanghai, China). In addition, electrochemical impedance spectroscopy (EIS) was also measured by the electrochemical workstation, which could evaluate the electron transfer ability of catalysts. To further analyze the interface interaction, in-situ Raman spectra of Co-ZFO@Mn-CN with O_3 were taken on a microscopic Raman spectrometer (IsoPlane SCT 320) with a 9 mW 633 nm laser light irradiation. Before analysis, the metal oxides were dispersed in the ozone water. Then the mixture was dropped on the slice for further detection.

2.4. Catalytic performance

The ozone reaction system consisted of a 250 mL cylindrical reactor, an O_3 supply plant and an exhaust treatment unit. Ozone was produced from pure oxygen by a laboratory ozone generator (Tonglin Technology, 3S-T3, China) (Scheme S2). The ozone diffuser was fixed at the center of the reactor bottom, which could make catalysts and O_3 uniformly dispersed in aqueous solution as ozone bubbling. As the common intermediate produced in organic pollutants degradation process, oxalic acid was difficultly mineralized completely, seriously limiting the treatment efficiency. Therefore much attention was paid on oxalic acid degradation [51, 57–60]. Herein, we considered OA as target pollutant which was used to evaluate the catalytic ozonation performance. In the typical semi-batch experiment, 200 mL of suspensions containing OA (50 mg/L) and 0.1 g catalysts were added into the reactor with O_3 bubbling through the ozone diffuser (flow rate = 100 mL/min, C = 25 mg/ L). At given time intervals, 2 mL of samples were withdrawn from the top of the reactor. To quench the residual ozone, 0.1 M Na$_2$S$_2$O$_3$ was added in the sample immediately. After filtration through a Millipore filter (pore size 0.22 μm), the residual OA concentration was determined. As the control experiment, same procedure was carried out without catalyst being added in. In addition, catalytic ozonation for other organic pollutants degradation [rhodamine B (RhB), Bisphenol A

(BPA), p-hydroxylbenzoic acid (PHBA), 1 H-Benzotriazole (BZA), 2, 4-Dichlorophenoxyacetic acid (2,4-D)] were also conducted to evaluate the catalytic performance of Co-ZFO@Mn-CN. The initial pH of reaction system was adjusted to 3 ± 0.1 by using HNO_3 (1.0 M). Furthermore, quenching experiments were conducted similarly as semi-batch experiment for oxalic acid degradation at pH 3, with dispersing certain quenching agent for ROS in 200 mL of suspensions containing OA (50 mg/L).

The gaseous ozone concentration was measured by an ozone analyzer (Tonglin Technology, 3S-J5000, China). OA concentration was analyzed by an ion chromatography (Dionex ICS-1100) with the mobile phase of 25 mM KOH (flow rate =1.0 mL/min). An UV–vis spectrophotometer (UV-1800, Shimadzu, Japan) was used to determine Rhodamine B (Rh B) concentration at the wavelength of 554 nm. The concentrations of BPA, PHBA, 2,4-D and BZA in solution were measured by a 1200 series HPLC equipped with a UV–visible detector and C-18 column (Eclipse XBD-C18, 4.5 ×150 mm, 5 μm). Detailed chromatographic conditions for different organics determination are listed in Table S1. The leaching concentration of metal ions from catalyst in solution was determined using a Perkin-Elmer Elan DRC-e ICP-MS instrument. Reaction oxygen species detections were performed by the electron paramagnetic resonance (EPR, Bruker, EMXPLUS, Germany) using DMPO and TEMP as the spin-trapping agent.

2.5. Theoretical calculation methods

DFT calculations were carried out using the Vienna Ab-initio Simulation Package (VASP) with the frozen-core all-electron projector-augment-wave (PAW) method [61–64]. VASP was generally used to simulate the interfacial interaction during the catalytic reaction [38,51,65], which could provide useful information of the catalytic mechanism. The Perdew-Burke-Ernzerh (PBE) of generalized gradient approximation (GGA) was adopted to describe the exchanges and correlation potentials [66]. The cutoff energy for the plane-wave basis set was set to 450 eV. A 3-layer 1×1 $ZnFe_{1.33}Co_{0.67}O_4$(311) slab was used, and a vacuum region of 15 Å above the slab was used to ensure the decoupling between neighboring systems. A 6×3 monolayer graphene terminated with H atom was used to build Mn-N_4-C slab. The O-vacancy $ZnFe_{1.33}Co_{0.67}O_4$(311) slab was built by delete one O atom in the surface of the slab. The monolayer Mn-N_4-C slab was placed on $ZnFe_{1.33}Co_{0.67}O_4$(311) slab to simulate Mn-N_4-C/$ZnFe_{1.33}Co_{0.67}O_4$ heterojunction. For the geometry optimization, the atoms in the bottom-layer of $ZnFe_{1.33}Co_{0.67}O_4$(311) slab were fixed to their bulk positions. The geometry optimizations were performed until the forces on each ion was reduced below 0.02 eV/Å, and the Gamma k-point sampling of the Brillouin zone were used [67].

The Gibbs free-energy (G) is calculated as Eq. 1.

$$G = E_{DFT} + E_{ZPE} - TS \tag{1}$$

where E_{DFT} is the DFT calculated energies, E_{ZPE} is the zero point energy, T is temperature, and S is molecule entropy.

3. Results and discussion

3.1. Characterization of catalysts

In most cases, the morphology of ZFO in TEM appeared nanoparticles [68–70], while Mn-CN appeared multiple sheets [71–73]. Herein, the typical core-shell structure of Co-ZFO@Mn-CN is observed in SEM image (Fig. 1a), and nano-hexagonal Co-ZFO with diameters of 20–60 nm is covered by Mn-CN (Fig. 1b). The interplanar spacing of 0.205 nm, 0.254 nm and 0.291 nm are ascribed to (400), (311) and (220) planes of Co-ZFO (Fig. 1c), respectively. Being attributed to the binding of the Mn-CN and Co-ZFO, both Co and Mn are uniformly dispersed in the composite of Co-ZFO@Mn-CN (Fig. 1d). Previous work reported that downsizing the metal species benefited their uniform dispersion on carbon-based supports [74], which facilitated the charge transfer from the metal to the supports because of the downshifted metal D-band
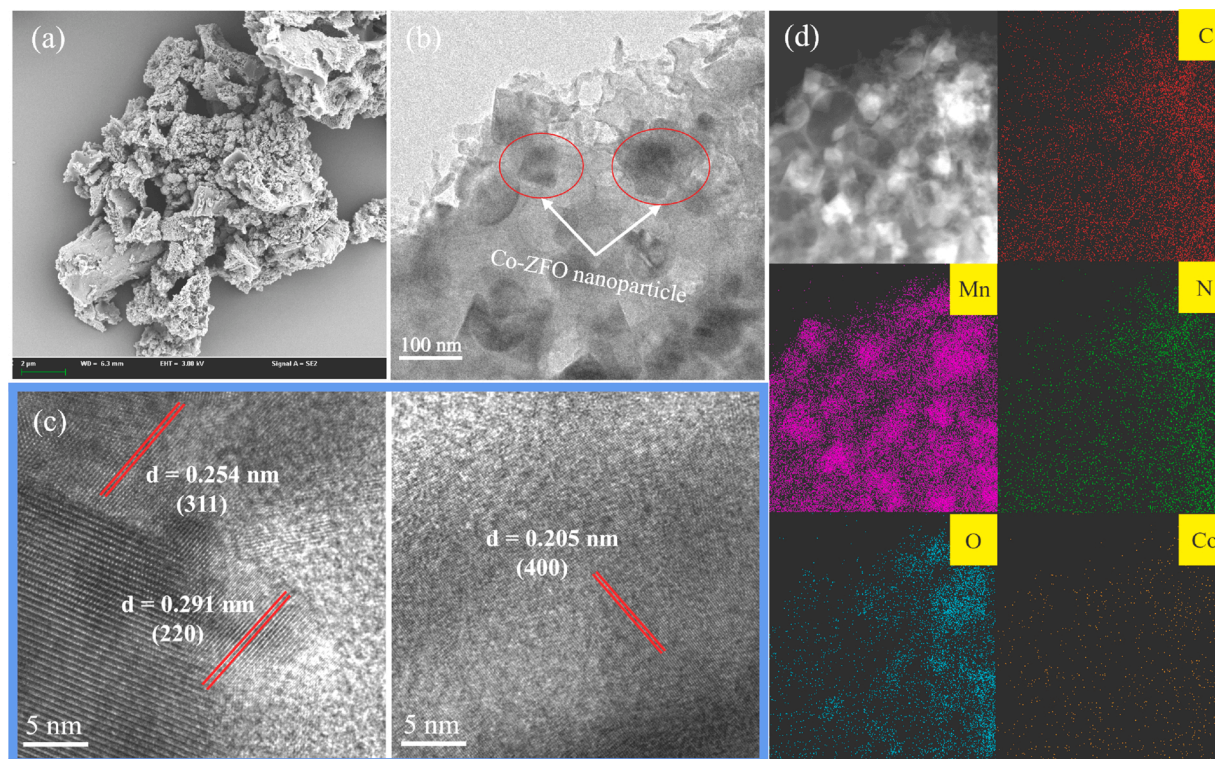

Fig. 1. (a) SEM image of Co-ZFO@Mn-CN; (b) TEM image of Co-ZFO@Mn-CN; (c) HRTEM images show the lattice fringe of Co-ZFO in Co-ZFO@Mn-CN; (d) Corresponding elemental mapping of C, Mn, N, O and Co for Co-ZFO@Mn-CN.

center.

XRD spectra of Co-ZFO@Mn-CN and other as-prepared samples are shown in Fig. 2. The strong peak ($2\theta = 27.5°$) referring to carbon (002) plane are observed in all samples (Fig. 2a), exhibiting similar structure to g-C_3N_4. Furthermore, as covered by Mn-CN, characteristic peak of Co planes [(311), (400) and (220)] are not observed in spectra of Co-ZFO@Mn-CN. Such core-shell structure has been verified in TEM (Fig. 1). Notably, the (311) plane exhibits high stabilization with a large degree of unsaturation, facilitating other metals doped in original structure. Due to formation of new Zn-O and Fe-O chemical bonds at two-fold Zn and three-fold Fe centers, O_3 preferred to be adsorbed and decomposed on (311) facets. In addition, peaks near 34.6° are ascribed to (111) facets of MnO, confirming the existence of Mn(II) in Mn-CN and

Co-ZFO@Mn-CN (Fig. 2b). Previous work reported that Mn(II)-N sites exhibited excellent electrochemical performance in oxygen reduction reaction [40,75]. The increased local DOS around the Fermi level by the formation of Mn-N coordination could enhance charge transfer and adsorption capacity, which played the important role in boosting the catalytic activities [34]. In addition, characteristic peaks of Co-ZFO [(220), (311), (400), (511) and (440) facets] shift slightly compared with ZFO (Fig. 2c), also confirming Co doped into the ZFO framework. Furthermore, as shown in FT-IR spectra of Mn-CN and Co-ZFO@Mn-CN (Fig. 2d), peak located at 808 cm^{-1} is ascribed to the out-of-plane bending vibrations of tri-striazine, while the characteristic absorption band between 1240 and 1640 cm^{-1} is caused by the stretching vibration of the C-N and C=N bonds. These characteristic peaks of C-N and C=N
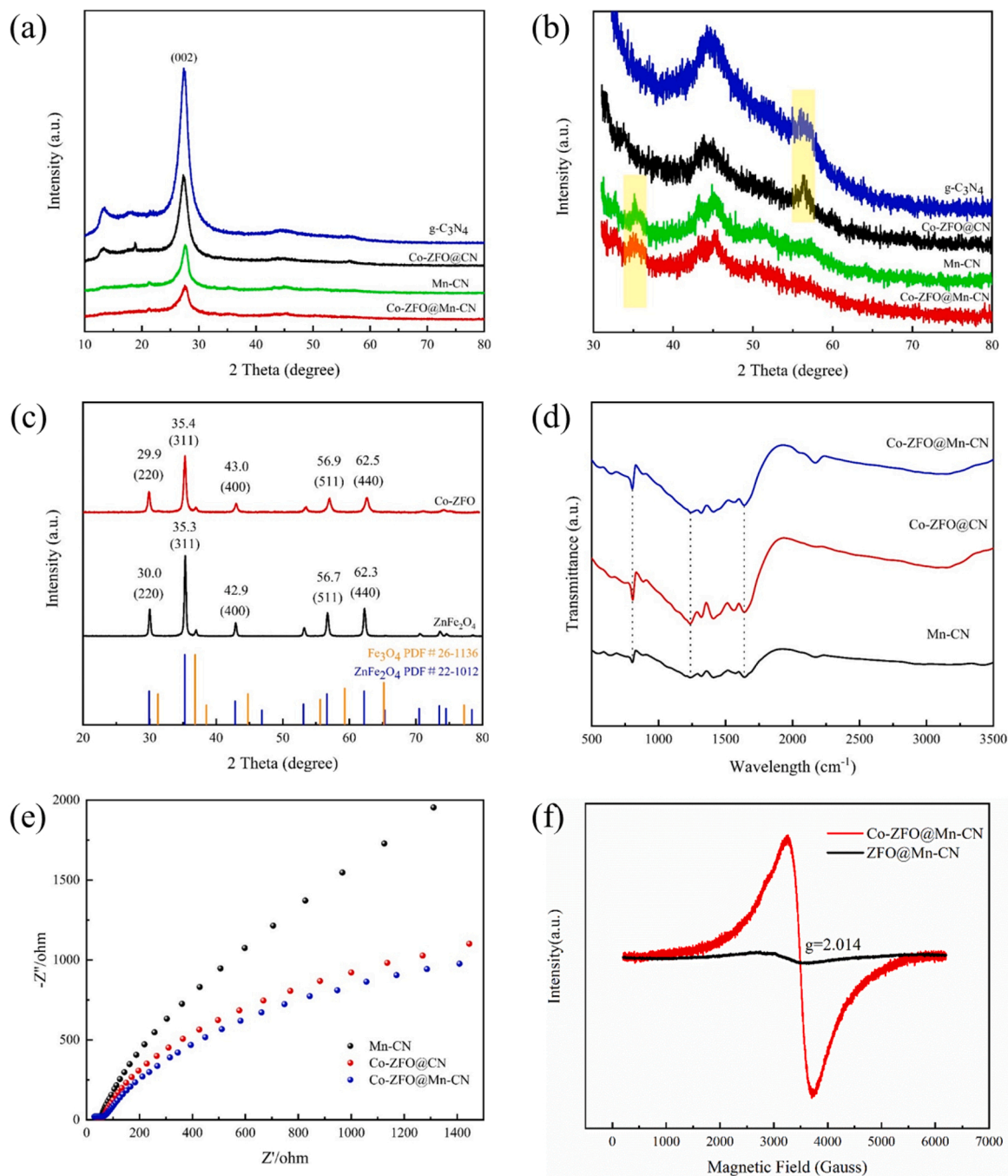

Fig. 2. (a) XRD patterns of several catalysts; (b) high resolution XRD of several catalysts; (c) XRD patterns of $ZnFe_2O_4$ and Co-ZFO and the standard PDF cards of Fe_3O_4 and $ZnFe_2O_4$; (d) FT-IR spectra images of several catalysts; (e) EIS of different catalysts; (f) Solid EPR spectra of Co-ZFO@Mn-CN.

suggested that samples contained the similar structured unit of carbon nitride.

Electrochemical impedance spectroscopy (EIS) can be used to evaluate the electron transfer processes, in which the larger semicircle diameter represents the higher resistance. In the present work, the Nyquist plot diameter of different samples follows the order of Mn-CN > Co-ZFO/CN > Co-ZFO@Mn-CN, suggesting the highest charge

transfer rate of Co-ZFO@Mn-CN (Fig. 2e). The carbon layer of Mn-CN provided Co-ZFO@Mn-CN with an electronic network which facilitated the charge transfer during the catalytic reaction. According to theoretical calculations, carbon nitride doped with Mn heteroatom possessed lower overpotential compared with graphitic-N and pyridinic-N [76]. In the ligand environment, low overpotential could influence the spin density and charge distribution of carbon atoms, resulting in
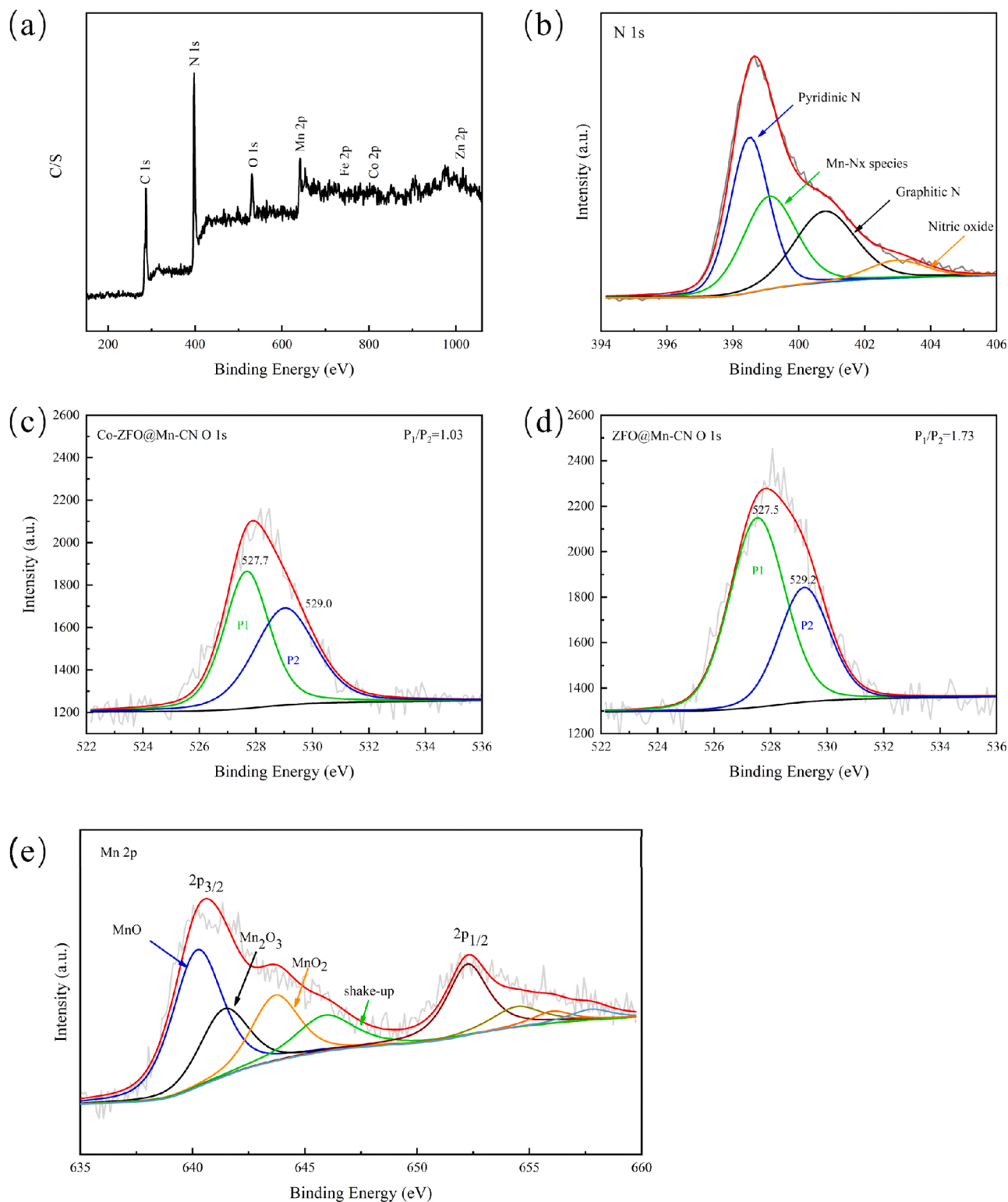

Fig. 3. (a) XPS survey spectra of Co-ZFO@Mn-CN; (b) N 1 s XPS spectra of Co-ZFO@Mn-CN; (c) O 1 s XPS spectra of Co-ZFO@Mn-CN; (d) O 1 s XPS spectra of ZFO@Mn-CN. (e) Mn 2p XPS spectra of Co-ZFO@Mn-CN before reaction.

enhancement of electrical conductivity. On the other hand, due to intrinsic electrophilicity, O_3 preferred to attack the electron-rich sites, and was subsequently dissociated into ROS [77]. As electron-rich region, OVs could adsorb O_3 and facilitate it conversion into $HO_2^\bullet/O_2^{\bullet-}$ and $^1O_2$. Herein, introduction of Co into catalysts induces the formation of OVs, which causes that intensity of the EPR signal (g = 2.014) for Co-ZFO@Mn-CN is much stronger than that for ZFO@Mn-CN (Fig. 2f) [78–82]. Consequently, large amounts of unpaired OVs-electrons accumulated on Co-ZFO@Mn-CN surface enable O_3 to be adsorbed and subsequently activated over Co-ZFO@Mn-CN [51].

XPS spectra could provide useful information about valence state and chemical bond of the catalysts surface. Based on the XPS survey of catalyst (Fig. 3a), N 1 s spectra can be deconvoluted into pyridinic N (398.5 eV), Mn-N_X species (399.1 eV), graphitic N (400.8 eV), and nitric oxide (NOx, 402.9 eV) (Fig. 3b) [75,82]. The obvious peak of Mn-N_X suggested the N strongly coordinated with Mn, which enable unconstrained electrons to be transferred between the Mn dopant and the carbon scaffold [34]. Besides, owing to higher electronegativity (3.04 eV) and smaller atom diameter (0.075 nm), N doped in carbon skeleton could increases the electron density of catalyst surface, facilitating the electrophilic interaction with O_3. As for O 1 s, peaks near 527 eV and 529 eV respectively correspond to lattice oxygen and surface oxygen (e.g. surface hydroxyl and other chemisorbed oxygen species) (Fig. 3c, d). Since lattice doping of Co induces the formation of OVs on catalysts surface (Fig. 2f), the lattice oxygen peak intensity of Co-ZFO@Mn-CN is much lower than that of ZFO@Mn-CN (Fig. 3d). According to the peak area ratio (R) of lattice O (P_1) to chemisorbed oxygen O species (P_2), the relative quantity of OVs on Co-ZFO@Mn-CN

(P_1/P_2 =1.03) is much higher than that on ZFO@Mn-CN (P_1/P_2 =1.73), which is consistent with the solid EPR result. In addition, peaks of Mn $2p_{3/2}$ (640.3 eV) and Mn $2p_{1/2}$ (652.4 eV) are identified in spectra of Co-ZFO@Mn-CN, along with two shake-up satellite peaks at 646.0 eV and 657.8 eV. Based on the integral areas of different Mn 2p peaks, it can be proposed that the proportion of MnO is much higher than those of Mn_2O_3 and MnO_2, which is also consistent with XRD results (Fig. 3e).

3.2. Catalytic performance

Catalytic ozonation of refractory organic pollutants OA are conducted to evaluate catalysts performances (Fig. 4a), which follow the order of Co-ZFO@Mn-CN/O_3 (95.2%) > Mn-CN/O_3 (81.4%) > Co-ZFO@CN/O_3 (72.7%) > Co-ZFO/O_3 (69.0%). Compared with other catalysts for ozonation reported in previous literatures (Table S2), Co-ZFO@Mn-CN/O_3 exhibits superior catalytic performance. In addition, the highest pseudo-first order reaction rate constant also suggests the excellent catalytic activity Co-ZFO@Mn-CN among these tested samples (Fig. 4b). As comparison, less than 5% of OA is removed without pumping O_3 in reactor while only 17.6% OA can be degraded in the absent of Co-ZFO@Mn-CN, demonstrating the crucial role of Co-ZFO@Mn-CN in O_3 activation process. Furthermore, satisfied reusability of Co-ZFO@Mn-CN (Fig. 4c) is observed in five successive experiments, and more than 80% of OA could be removed even after 4th cycles. In addition, according to the standard of EPA [Fe (0.3 mg/L), Mn (0.05 mg/L), Zn (5 mg/L)], the slight leaching of Fe (0.09 mg/L), Mn (0.03 mg/L) and Zn (0.05 mg/L) detected in successive experiments could be negligible (Table S3). Such perfect stability of Co-ZFO@Mn-CN
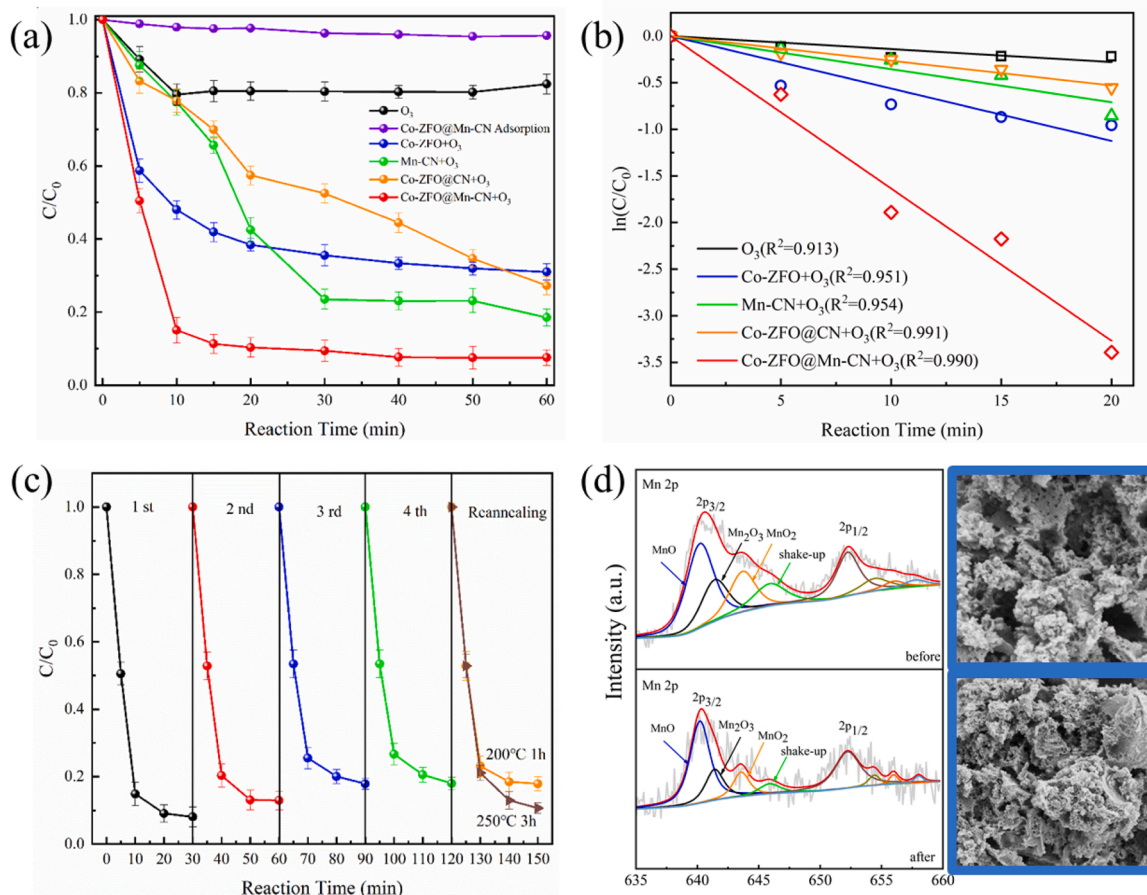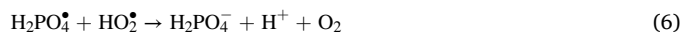

Fig. 4. (a) Ozonation and catalytic ozonation with several catalysts; (b) Pseudo-first-order equation fit the kinetic degradation curves of OA degradation over different catalysts; (c) Catalytic stability and reannealing tests of Co-ZFO@Mn-CN for degrading OA; (d) SEM images and Mn 2p XPS spectra of Co-ZFO@Mn-CN before and after reaction. Reaction conditions: $[OA]_0$ = 50 mg/L; catalyst loading = 0.5 g/L; ozone flow rate, 100 mL/min; ozone concentration, 25 mg/L; solution pH = 3.

might be ascribed to the protection of Mn-CN shell and strong interaction of Mn-N bond. In the XPS spectra of Co-ZFO@Mn-CN, the integral area of Mn(II) and Mn(III) are not changed obviously after catalytic reaction, which indicates that these Mn sites still maintain the reducibility for O_3 activation (Fig. 4d). Besides, SEM images demonstrate that Co-ZFO@Mn-CN morphology and structure are not destroyed after successive experiments, which are consistent with the OA degradation performance and XPS spectra. On the other hand, although slight decrease of catalytic activity occurred inevitably during the multiple recycle use, catalytic activity of Co-ZFO@Mn-CN can be effectively recovered by annealing. Increase of reannealing temperature and time can slightly enhance the regeneration efficiency (Fig. 4c). Thus, Co-ZFO@Mn-CN remains high removal rate of OA after the reannealing treatment (250 ℃, 3 h) (Fig. S1).

As important experiment parameters, reaction temperature and water quality generally influenced the catalysts activities. Herein, although increase the temperature could accelerate the mass transfer and reaction kinetics, 25 ℃ is selected as the optimal reaction temperature in considering of the energy consumption and O_3 solubility (Fig. 5a). Besides, OA degradation is inhibited in the presence of low concentration anions (0.1 mM) with their influences following the order of $Cl^- > H_2PO_4^- > SO_4^{2-}$ (Fig. 5b). The most adverse effect of Cl^- to catalytic ozonation reaction could be explained as follows: (1) Cl^- competed with OA for active sites of catalysts; (2) $Cl^\bullet$ produced from the reaction of $\bullet OH$ and Cl^-, could possess lower oxidation activity compared with $\bullet OH$ (Eq.2) [83]; (3) $\bullet O_2^-$ was consumed by the reaction with $\bullet Cl_2^-$ (Eqs. 3–4) [84]. In addition, dihydrogen phosphate ions also exhibited inhibitory effect in ozone decomposition, which could be

explained as follows: (1) dihydrogen phosphate ions bound on catalyst surface, decreasing heterogeneous activation of ozone considerably; (2) addition of $H_2PO_4^-$ could quench the $HO_2^\bullet$ in a certain degree (Eqs. 5–6) [85,86], which showed adverse effect on OA degradation. As for SO_4^{2-}, its weak competition with OA molecules for active sites caused a slight decrease of OA degradation rate.

$$\bullet OH + Cl^- \rightarrow Cl^\bullet + OH^- \tag{2}$$

$$Cl^- + \bullet Cl \rightarrow \bullet Cl_2^- \tag{3}$$

$$\bullet Cl_2^- + \bullet O_2^- \rightarrow 2Cl^- + O_2 \tag{4}$$

$$\bullet OH + H_2PO_4^- \rightarrow OH^- + H_2PO_4^\bullet \tag{5}$$

$$H_2PO_4^\bullet + HO_2^\bullet \rightarrow H_2PO_4^- + H^+ + O_2 \tag{6}$$

In order to evaluate the application potential in wastewater treatment, catalytic degradations of various organic pollutants over Co-ZFO@Mn-CN/O_3 are conducted, including rhodamine B (RhB), Bisphenol A (BPA), p-hydroxylbenzoic acid (PHBA), 1 H-Benzotriazole (BZA) and 2,4-Dichlorophenoxyacetic acid (2,4-D) (Fig. 5c). More than 70% organics can be removed (100.0% for RhB, 86.7% for BPA, 91.2% for PHBA, 81.5% for BZA, 74.2% for 2,4-D) within 60 min. And the mineralization rate followed the order of RhB (99%) > PHBA (90%) > BPA (85%) > BZA (81%) > 2,4-D (73%), which was much higher than traditional catalytic ozonation process [87–89]. Owing to higher electron density, RhB benzenes are preferred to be adsorbed and attacked by ROS, resulting in the highest degradation rate over Co-ZFO@Mn-CN/O_3. On the contrary, the substitution of chlorine on benzene ring decreased
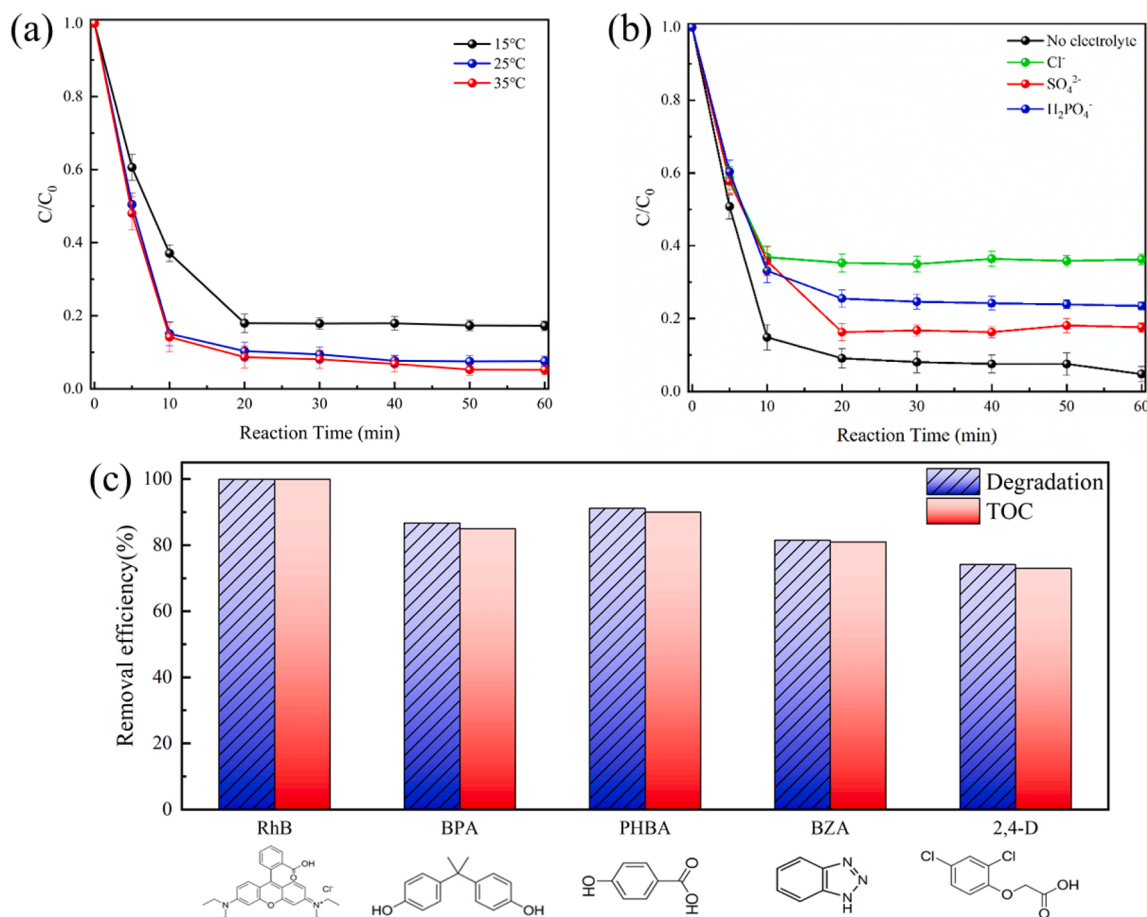

Fig. 5. (a) OA removal with Co-ZFO@Mn-CN under different solution temperatures; (b) In the presence of inorganic anions (Cl^-, SO_4^{2-}, $H_2PO_4^-$) with the initial anion concentration of 0.1 mM; (c) Removal of different pollutants by the Co-ZFO@Mn-CN ozonation catalytic system. Reaction conditions: [pollutants]$_0$ = 50 mg/L; catalyst loading = 0.5 g/L; ozone flow rate, 100 mL/min; ozone concentration, 25 mg/L, solution pH = 3.

the electron density of 2,4-D, which made the adverse effect to ROS adsorption and oxidation. Consequently, Co-ZFO@Mn-CN/O$_3$ achieved the relatively low degradation rate of 2,4-D. In addition, the intermediates of these organic pollutants during catalytic ozonation process are analyzed by using LC-MS, which demonstrated that all these organics pollutants degradations follow the similar pathway including the hydroxylation/carbonylation, benzene ring cleavage, carboxylation and decarboxylation (Fig. S2 - S6).

3.3. Possible catalytic mechanism

Quenching experiments were performed to identify the ROS responsible to OA degradation (Fig. 6a). In the presence of t-BA (scavenger for $^\bullet$OH), the removal rate of OA was not decreased obviously, which demonstrated that $^\bullet$OH was not the main active species for OA degradation. On the contrary, addition of p-BQ seriously inhibited OA degradation, suggesting $O_2^{\bullet-}$ played an important role in OA removal. Considering both radicals [$HO_2^\bullet/O_2^{\bullet-}$ ($kO_2^{\bullet-} = 3.5 - 7.8 \times 10^8$ M$^{-1}\cdot$s^{-1}), $^\bullet$OH ($kHO^\bullet = 1.2 \times 10^9$ M$^{-1}\cdot$s^{-1})] and O_3 ($kO_3 = 2.5 \times 10^3$ M$^{-1}\cdot$s^{-1}) could react with p-BQ, OA degradation in the presence of different
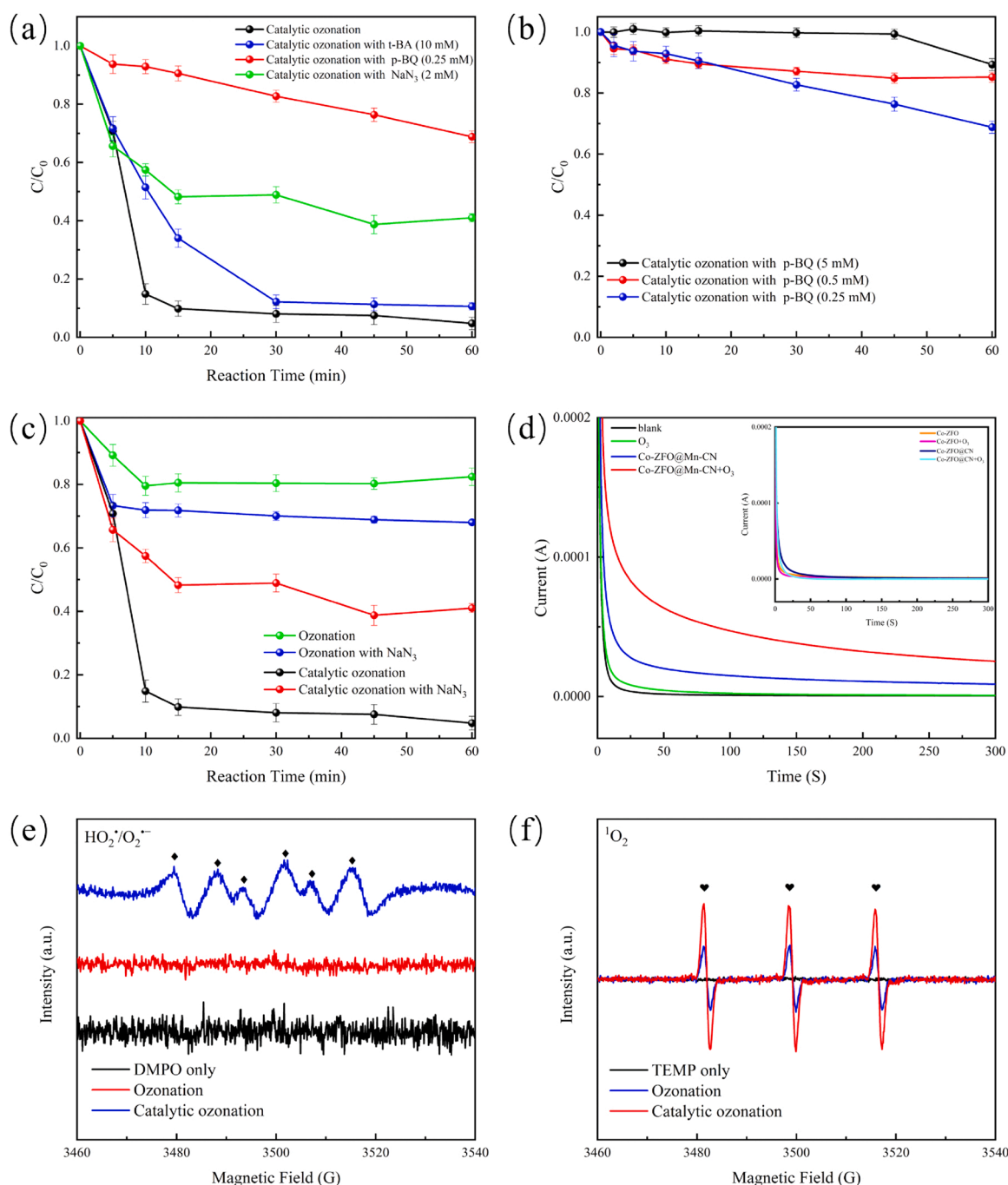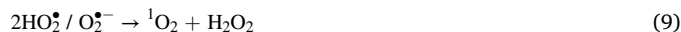

Fig. 6. (a) Effect of different radical scavengers on OA degradation; (b) The various concentration of p-BQ for catalytic ozonation; (c) Effect of NaN$_3$ on OA degradation; (d) Chronoamperometry curves in blank solution, blank solution with catalysts, O$_3$ solution, and O$_3$ solution with catalysts; (e) EPR spectra employing DMPO as the trapping agent with methanol as reaction medium; (f) EPR spectra utilizing TEMP as the trapping agent with ultrapure water as reaction medium. Reaction conditions: [OA]$_0$ = 50 mg/L; catalyst loading = 0.5 g/L; ozone flow rate, 100 mL/min; ozone concentration, 25 mg/L, solution pH = 3.

concentration p-BQ were carried out to exclude the influence of •OH and O_3. The results indicate that removal efficiency of OA declined from 89% to 69% even in the presence of low concentration p-BQ (0.25 mM) (Fig. 6b), which confirms the main ROS of $O_2^{•-}$ in the system of Co-ZFO@Mn-CN/O_3. In addition, NaN_3 was commonly used to quench $^1O_2$ because the kinetic rate constant followed the order of NaN_3 (2×10^9 $M^{-1} s^{-1}$) > FFA (1.2×10^8 $M^{-1} s^{-1}$) > p-BQ (6.6×10^7 $M^{-1} s^{-1}$) > TBA (1.8×10^3 $M^{-1} s^{-1}$) [90–98]. As NaN_3 is added in the reaction system of O_3/Co-ZFO@Mn-CN, OA degradation is obviously inhibited, suggesting that $^1O_2$ (redox potential of 0.85 V) is also identified as the main ROS (Fig. 6c). Notably, although addition of NaN_3 consumed the O_3, $Na_2C_2O_4$ produced from the reaction of OA and NaN_3 ($NaN_3 + H_2O \rightarrow HN_3 + NaOH$; $2NaOH + H_2C_2O_4 \rightarrow Na_2C_2O_4 + 2 H_2O$) with poor stability was more easily to be degraded compared with OA. Thus, addition of NaN_3 enhanced OA degradation in a certain degree without Co-ZFO@Mn-CN. As for the reaction system of O_3/Co-ZFO@Mn-CN, even with the improvement of OA degradation caused by production of $Na_2C_2O_4$, addition of NaN_3 still seriously inhibited OA degradation because large amounts of $^1O_2$ was quenched. Thus, both $O_2^{•-}$ and $^1O_2$ played dominant role in OA degradation.

On the other hand, in most cases •OH and $O_2^{•-}$ were detected as main ROS during the catalytic ozonation [23,45], and only small portion of $HO_2^{•}/O_2^{•-}$ could be convert into H_2O_2 and $^1O_2$ via radical recombination [77,99]. Herein, in situ EPR technique is employed to directly identify the ROS using DMPO and TEMP as spin trapping agents (Fig. 6e, f). Characteristics peaks of DMPO-$^•$OOH adducts observed in the system of Co-ZFO@Mn-CN/O_3 suggested the production of $O_2^{•-}$. Meanwhile, the appearance of strong triplet TEMPO signals represents large amounts of $^1O_2$ generated from radical recombination (Fig. 6f), which is consistent with the quenching experiments results. In addition, the signal of •OH is much weaker compared with $O_2^{•-}$ and $^1O_2$ (Fig. S7), suggesting the generation of •OH did not play the important role in this reaction system. Furthermore, in the chronoamperometry curves, the oxidation current is increased in electrolyte solution with O_3 bubbling after adding Co-ZFO@Mn-CN (Fig. 6d), while neglect changes of oxidation current are observed in blank solution before and after adding Co-ZFO@Mn-CN. It suggested that some weak oxidants such as $HO_2^{•}/O_2^{•-}$ produced from the reaction between Co-ZFO@Mn-CN and O_3, preferred to be oxidized over Co-ZFO@Mn-CN with an obvious rise of oxidation current.

Furthermore, DFT calculations were performed to illustrate ROS generation and transformation mechanism over Co-ZFO@Mn-CN. Possible catalytic reaction pathways and corresponding energy changes are provided in Fig. 7. In the first reaction step (R1), O_3 adsorbed on OVs with the adsorption energies of − 2.14 eV cause the significant extension of O-O bond length in O_3 from 1.284 to 2.212 Å (Fig. S8). Owing to the strong Lewis acidic property of OVs and the stretched O-O bond length in O_3, the O_3 was spontaneously dissociated [51,100,101], and subsequently decomposed into $^*O_{ad}$ and O_2 (Eq. 7) involving an exothermal reaction with a free energy release of 2.06 eV (Fig. 7b). Meanwhile, $^*O_{ad}$ could subsequently reacted with dissolved O_3 to produce large amounts of $HO_2^{•}$ (Eq. 8), accompanying with the production of $^1O_2$ and H_2O_2 via recombination of $HO_2^{•}$ (Eq. 9) (Fig. 7a). The production of these ROS has been proved by EPR signals (Fig. 6e, f). For the second reaction step (R2) (Fig. 7b), HOO^-, which is generated from the deprotonation of H_2O_2, prefers to form HOO-Mn-N_X bonds with Co-ZFO@Mn-CN because of relatively lower free energy (Fig. 7b). In the in-situ Raman spectra of Co-ZFO@Mn-CN with O_3 (Fig. S9), typical peak at 828 cm^{-1} is ascribed to the adsorbed −OOH species on Co-ZFO@Mn-CN surface, which provides the evidence for HOO-Mn-N_X bonds in the synthesized catalyst [102–105]. DFT calculation indicates that this formation process of HOO-Mn-N_X bonds could release more free energy (1.31 eV) than the process of H_2O_2 adsorbed on Co-ZFO@Mn-CN (0.28 eV). And in the third reaction step (R3) (Fig. 7b), HOO-Mn-N_X bonds is broken under the attack of O_3 with the generation of $HO_2^{•}$ and $HO_3^{•}/O_3^{•-}$ involving an exothermal reaction. As calculated in DFT theory, a free energy of 3.12 eV is released in this bond-breaking process, while H_2O_2 desorbed from Co-ZFO@Mn-CN is an endothermic reaction (1.31 eV) (Fig. 7b). Owing to its stronger oxidizing ability (E_0 = 2.07 V_{NHE}) compared to that of $HO_2^{•}$ (E_0 = 1.44 V_{NHE}), O_3 could help to break the $HOO−Mn−N_x$ bond with the production of $HO_2^{•}$ and $HO_3^{•}/O_3^{•-}$. Thus, the decomposition of $HOO−Mn−N_x$ proceeded much more easily with the aid of O_3, accelerating $HO_2•$ and $HO_3^{•}/O_3^{•-}$ generation. Subsequently, $HO_3^{•}/O_2^{•-}$ are generated (Eqs. 10–11) and converted to $^1O_2$ (Eq.9) for organics degradation.

$$O_3 \xrightarrow{activate} *O_{ad} + O_2 \tag{7}$$

$$*O_{ad} + O_3 + H_2O \rightarrow O_2 + HO_2^{•} \tag{8}$$

$$2HO_2^{•} / O_2^{•-} \rightarrow {}^1O_2 + H_2O_2 \tag{9}$$

$$O_3^{•-} + H_2O \rightarrow HO_3^{•} + OH^- \tag{10}$$

$$HO_3^{•} \rightarrow O_2^{•-} + HO• \tag{11}$$

Based on the above analysis, O_3 could be activated both on OVs and
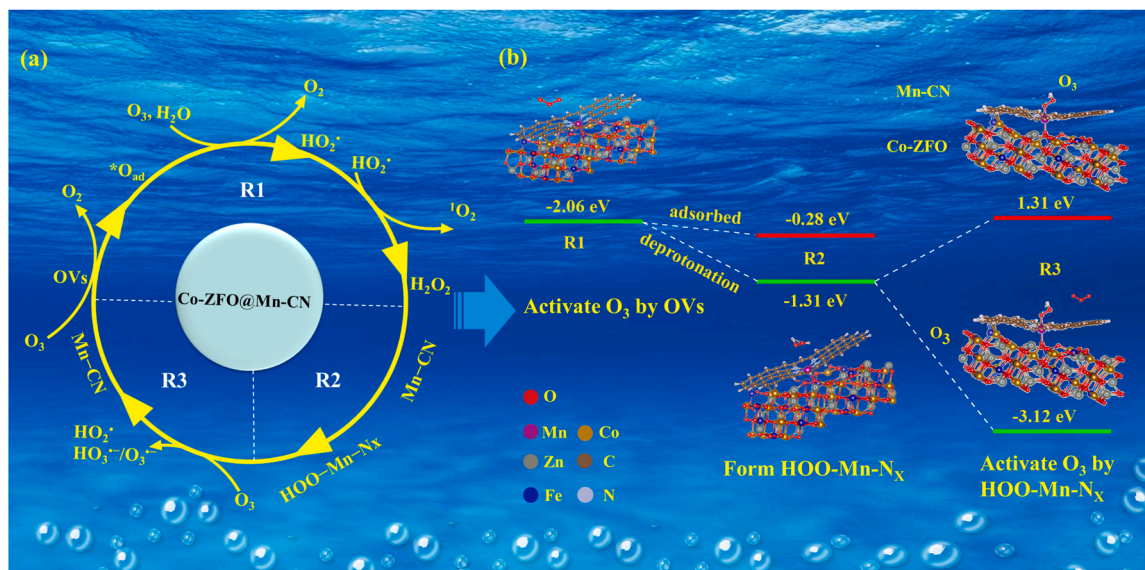

Fig. 7. (a) Catalytic ozonation mechanism over Co-ZFO@Mn-CN; (b) Free energy changes of ozone molecule and Co-ZFO@Mn-CN during the catalytic reaction.

HOO-Mn-N$_X$ bonds. On one hand, O$_3$ adsorbed by OVs could induce the chain reactions with the production of ^{1}O$_2$ and H$_2$O$_2$. On the other hand, the produced H$_2$O$_2$ could be further deprotonated to form HOO-Mn-N$_X$ with Co-ZFO@Mn-CN. Notably, HOO-Mn-N$_X$ bond could react with O$_3$ to generate HO$_2^\bullet$ and O$_3^{\bullet-}$. Such reactions induced by OVs and HOO-Mn-N$_X$ mentioned above not only promoted O$_3$ conversion into ROS for organics degradation, but also avoided inactivation of catalyst caused by Mn(II) sites oxidation. Thus we concluded that OVs and HOO-Mn-N$_X$ bonds showed the synergistic effects in ROS generation and organics degradation at room temperature.

4. Conclusion

In the present work, Co doped ZnFe$_2$O$_4$/Mn-CN hybrids (Co-ZFO@Mn-CN) was constructed with ^{1}O$_2$ and O$_2^{\bullet-}$ as main ROS for improvement of catalytic ozonation. The EPR results and XPS analysis suggested that both OVs and Mn-CN in Co-ZFO@Mn-CN were main active sites. DFT simulations further revealed that OVs in Co-ZFO@Mn-CN could provide abundant localized electrons for O$_3$ activation with the generation of large amounts of O$_2^{\bullet-}$. Subsequently, ^{1}O$_2$ and H$_2$O$_2$ were produced by the recombination of HO$_2^\bullet$/O$_2^{\bullet-}$. Notably, as the deprotonation product of H$_2$O$_2$, HOO$^-$ could form HOO-Mn-N$_X$ bonds with Co-ZFO@Mn-CN which preferred to be broken under the attack of O$_3$ with the generation of HO$_2^\bullet$ and HO$_3^\bullet$/O$_3^{\bullet-}$ involving a spontaneous exothermal reaction, avoiding the oxidation of transition metal. Combining advantages mentioned above, more than 70% organics could be mineralized, which was much higher than traditional catalytic ozonation process. Thus, this work provided an efficient way for enhancing the utilization of O$_3$ and ROS by inducing formation of OVs and HOO-Mn-N$_X$ bonds.

CRediT authorship contribution statement

Menglu Xu: Methodology, Data curation, Investigation, Writing – review & editing. **Yibing Zhang:** Conceptualization, Data curation, Investigation, Writing – original draft. **Huaqin Yin:** Formal analysis, Methodology. **Jinnan Wang:** Conceptualization, Project administration, Supervision, Writing – review & editing. **Aimin Li:** Supervision. **Philippe François-Xavier Corvini:** Writing – review & editing. All authors have read and agreed to the published version of the manuscript.

Declaration of Competing Interest

The authors declare that they have no known competing financial interests or personal relationships that could have appeared to influence the work reported in this paper.

Data Availability

No data was used for the research described in the article.

Acknowledgements

Appendix A. Supporting information

Supplementary data associated with this article can be found in the online version at doi:10.1016/j.apcatb.2022.122085.

References

[1] H. Lu, Z. Zhu, H. Zhang, J. Zhu, Y. Qiu, L. Zhu, S. Kuppers, Fenton-like catalysis and oxidation/adsorption performances of acetaminophen and arsenic pollutants in water on a multimetal Cu-Zn-Fe-LDH, ACS Appl. Mater. Interfaces 8 (2016) 25343–25352.

[2] W. Liu, Y. Wang, Z. Ai, L. Zhang, Hydrothermal synthesis of FeS$_2$ as a high-efficiency Fenton reagent to degrade alachlor via superoxide-mediated Fe(II)/Fe (III) cycle, ACS Appl. Mater. Interfaces 7 (2015) 28534–28544.

[3] Y. Wang, H. Sun, H.M. Ang, M.O. Tade, S. Wang, Facile synthesis of hierarchically structured magnetic MnO$_2$/ZnFe$_2$O$_4$ hybrid materials and their performance in heterogeneous activation of peroxymonosulfate, ACS Appl. Mater. Interfaces 6 (2014) 19914–19923.

[4] J. Hu, P. Zhang, W. An, L. Liu, Y. Liang, W. Cui, In-situ Fe-doped g-C$_3$N$_4$ heterogeneous catalyst via photocatalysis-Fenton reaction with enriched photocatalytic performance for removal of complex wastewater, Appl. Catal. B Environ. 245 (2019) 130–142.

[5] Y. Zhu, R. Zhu, Y. Xi, J. Zhu, G. Zhu, H. He, Strategies for enhancing the heterogeneous Fenton catalytic reactivity: a review, Appl. Catal. B Environ. 255 (2019), 117739.

[6] R. Yamaguchi, S. Kurosu, M. Suzuki, Y. Kawase, Hydroxyl radical generation by zero-valent iron/Cu (ZVI/Cu) bimetallic catalyst in wastewater treatment: heterogeneous Fenton/Fenton-like reactions by Fenton reagents formed in-situ under oxic conditions, Chem. Eng. J. 334 (2018) 1537–1549.

[7] Y. Liu, Y. Zhao, J. Wang, Fenton/Fenton-like processes with in-situ production of hydrogen peroxide/hydroxyl radical for degradation of emerging contaminants: advances and prospects, J. Hazard. Mater. 404 (2021), 124191.

[8] A.V. Vorontsov, Advancing Fenton and photo-Fenton water treatment through the catalyst design, J. Hazard. Mater. 372 (2019) 103–112.

[9] Y. Zhang, M. Zhou, A critical review of the application of chelating agents to enable Fenton and 1 Fenton-like reactions at high pH values, J. Hazard. Mater. 362 (2019) 436–450.

[10] K. Li, L. Xu, Y. Zhang, A. Cao, Y. Wang, H. Huang, J. Wang, A novel electro-catalytic membrane contactor for improving the efficiency of ozone on wastewater treatment, Appl. Catal. B Environ. 249 (2019) 316–321.

[11] J. Cai, M. Zhou, Q. Zhang, Y. Tian, G. Song, The radical and non-radical oxidation mechanism of electrochemically activated persulfate process on different cathodes in divided and undivided cell, J. Hazard. Mater. 416 (2021), 125804.

[12] L. Labiadh, M.A. Oturan, M. Panizza, N.B. Hamadi, S. Ammar, Complete removal of AHPS synthetic dye from water using new electro-Fenton oxidation catalyzed by natural pyrite as heterogeneous catalyst, J. Hazard. Mater. 297 (2015) 34–41.

[13] B. Unnikrishnan, V. Mani, S.-M. Chen, Highly sensitive amperometric sensor for carbamazepine determination based on electrochemically reduced graphene oxide–single–walled carbon nanotube composite film, Sens. Actuators B 173 (2012) 274–280.

[14] H. Song, L. Yan, Y. Wang, J. Jiang, J. Ma, C. Li, G. Wang, J. Gu, P. Liu, Electrochemically activated PMS and PDS: radical oxidation versus nonradical oxidation, Chem. Eng. J. 391 (2020), 123560.

[15] H. Wang, Y. Zhou, J. Wang, A. Li, P. François-Xavier, Corvini, BiOBr/Bi$_4$O$_5$Br$_2$/ PDI constructed for visible-light degradation of endocrine disrupting chemicals: synergistic effects of bi-heterojunction and oxygen evolution, Chem. Eng. J. 433 (2022), 133622.

[16] S. Song, B. Cheng, N. Wu, A. Meng, S. Cao, J. Yu, Structure effect of graphene on the photocatalytic performance of plasmonic Ag/Ag$_2$CO$_3$-rGO for photocatalytic elimination of pollutants, Appl. Catal. B Environ. 181 (2016) 71–78.

[17] W. Zhao, Y. Liu, Z. Wei, S. Yang, H. He, C. Sun, Fabrication of a novel p-n heterojunction photocatalyst n-BiVO$_4$@p-MoS$_2$ with core-shell structure and its excellent visible-light photocatalytic reduction and oxidation activities, Appl. Catal. B Environ. 185 (2016) 242–252.

[18] M. Mehrjouei, S. Müller, D. Möller, A review on photocatalytic ozonation used for the treatment of water and wastewater, Chem. Eng. J. 263 (2015) 209–219.

[19] W. Zhao, J. Zhang, F. Zhu, F. Mu, L. Zhang, B. Dai, J. Xu, A. Zhu, C. Sun, D.Y. C. Leung, Study the photocatalytic mechanism of the novel Ag/p-Ag$_2$O/n-BiVO$_4$ plasmonic photocatalyst for the simultaneous removal of BPA and chromium(VI), Chem. Eng. J. 361 (2019) 1352–1362.

[20] J. Zhu, Z. Yin, D. Yang, T. Sun, H. Yu, H.E. Hoster, H.H. Hng, H. Zhang, Q. Yan, Hierarchical hollow spheres composed of ultrathin Fe$_2$O$_3$ nanosheets for lithium storage and photocatalytic water oxidation, Energy Environ. Sci. 6 (2013) 987–993.

[21] B.C. Hodges, E.L. Cates, J.H. Kim, Challenges and prospects of advanced oxidation water treatment processes using catalytic nanomaterials, Nat. Nanotechnol. 13 (2018) 642–650.

[22] L. Zhu, J. Ji, J. Liu, S. Mine, M. Matsuoka, J. Zhang, M. Xing, Designing 3D-MoS$_2$ sponge as excellent cocatalysts in advanced oxidation processes for pollutant control, Angew. Chem. Int. Ed. Engl. 59 (2020) 13968–13976.

[23] S. Li, X. Li, H. Wu, X. Sun, F. Gu, L. Zhang, H. He, L. Li, Mechanism of synergistic effect on electron transfer over Co-Ce/MCM-48 during ozonation of pharmaceuticals in water, ACS Appl. Mater. Interfaces 11 (2019) 23957–23971.

[24] D. Wang, H. Xu, J. Ma, X. Lu, J. Qi, S. Song, Morphology control studies of MnTiO$_3$ nanostructures with exposed {0001} facets as a high-performance catalyst for water purification, ACS Appl. Mater. Interfaces 10 (2018) 31631–31640.

[25] S. Saeid, P. Tolvanen, N. Kumar, K. Eränen, J. Peltonen, M. Peurla, J.-P. Mikkola, A. Franz, T. Salmi, Advanced oxidation process for the removal of ibuprofen from aqueous solution: a non-catalytic and catalytic ozonation study in a semi-batch reactor, Appl. Catal. B Environ. 230 (2018) 77–90.

[26] S. Zhang, X. Quan, D. Wang, Catalytic ozonation in arrayed zinc oxide nanotubes as highly efficient mini-column catalyst reactors (MCRs): augmentation of hydroxyl radical exposure, Environ. Sci. Technol. 52 (2018) 8701–8711.

[27] K. Wei, X. Cao, W. Gu, P. Liang, X. Huang, X. Zhang, Ni-induced C-Al$_2$O$_3$-framework (NiCAF) supported core-multishell catalysts for efficient catalytic ozonation: a structure-to-performance study, Environ. Sci. Technol. 53 (2019) 6917–6926.

[28] A. Ikhlaq, D.R. Brown, B. Kasprzyk-Hordern, Mechanisms of catalytic ozonation: an investigation into superoxide ion radical and hydrogen peroxide formation during catalytic ozonation on alumina and zeolites in water, Appl. Catal. B Environ. 129 (2013) 437–449.

[29] D. Liu, C.R. Wang, Y.F. Song, Y.H. Wei, L. He, B.R. Lan, X.W. He, J.B. Wang, Effective mineralization of quinoline and bio-treated coking wastewater by catalytic ozonation using CuFe$_2$O$_4$/sepiolite catalyst: efficiency and mechanism, Chemosphere 227 (2019) 647–656.

[30] J. Wang, X. Quan, S. Chen, H.T. Yu, G.B. Liu, Enhanced catalytic ozonation by highly dispersed CeO$_2$ on carbon nanotubes for mineralization of organic pollutants, J. Hazard. Mater. 368 (2019) 621–629.

[31] Y.T. Zhang, Y.J. Xia, Q.W. Li, F. Qi, B.B. Xu, Z.L. Chen, Synchronously degradation benzotriazole and elimination bromate by perovskite oxides catalytic ozonation: performance and reaction mechanism, Sep. Purif. Technol. 197 (2018) 261–270.

[32] J.L. Wang, Z.Y. Bai, Fe-based catalysts for heterogeneous catalytic ozonation of emerging contaminants in water and wastewater, Chem. Eng. J. 312 (2017) 79–98.

[33] N.Z.B. Azali, A.A.H. Kadhum, A.A. AlAmiery, Free catalyzed synthesis of 2,2-bipyridine via ozonolysis technique, Ozone Sci. Eng (2017) 417–422.

[34] Y. Wang, X. Duan, Y. Xie, H. Sun, S. Wang, Nanocarbon-based catalytic ozonation for aqueous oxidation: engineering defects for active sites and tunable reaction pathways, ACS Catal. 10 (2020) 13383–13414.

[35] Y. Guo, Y. Zhang, G. Yu, Y. Wang, Revisiting the role of reactive oxygen species for pollutant abatement during catalytic ozonation: the probe approach versus the scavenger approach, Appl. Catal. B Environ. 280 (2021), 119418.

[36] A. Ikhlaq, D.R. Brown, B. Kasprzyk-Hordern, Mechanisms of catalytic ozonation: an investigation into superoxide ion radical and hydrogen peroxide formation during catalytic ozonation on alumina and zeolites in water, Appl. Catal. B Environ. 129 (2013) 437–449.

[37] S. Li, J. Wang, Y. Ye, Y. Tang, X. Li, F. Gu, L. Li, Composite Si-O-metal network catalysts with uneven electron distribution: enhanced activity and electron transfer for catalytic ozonation of carbamazepine, Appl. Catal. B Environ. 263 (2020), 118311.

[38] J. Ma, X. Li, C. Zhang, Q. Ma, H. He, Novel CeMn$_a$O$_x$ catalyst for highly efficient catalytic decomposition of ozone, Appl. Catal. B Environ. 264 (2020), 118498.

[39] R.C. Martins, R.M. Quinta-Ferreira, Catalytic ozonation of phenolic acids over a Mn-Ce-O catalyst, Appl. Catal. B Environ. 90 (2009) 268–277.

[40] H. Wang, Z. Huang, Z. Jiang, Z. Jiang, Y. Zhang, Z. Zhang, W. Shangguan, Trifunctional C@MnO catalyst for enhanced stable simultaneously catalytic removal of formaldehyde and ozone, ACS Catal. 8 (2018) 3164–3180.

[41] J. Xu, Y. Li, M. Qian, J. Pan, J. Ding, B. Guan, Amino-functionalized synthesis of MnO$_2$-NH$_2$-GO for catalytic ozonation of cephalexin, Appl. Catal. B-Environ. 256 (2019), 117797.

[42] C. He, Y. Wang, Z. Li, Y. Huang, Y. Liao, D. Xia, S.C. Lee, Facet engineered alpha-MnO$_2$ for efficient catalytic ozonation of odor CH$_3$SH: oxygen vacancy-induced active centers and catalytic mechanism, Environ. Sci. Technol. (2020) 12771–12783.

[43] D. Xia, W. Xu, Y. Wang, J. Yang, Y. Huang, L. Hu, C. He, D. Shu, D.Y.C. Leung, Z. Pang, Enhanced performance and conversion pathway for catalytic ozonation of methyl mercaptan on single-atom Ag deposited three-dimensional ordered mesoporous MnO$_2$, Environ. Sci. Technol. 52 (2018) 13399–13409.

[44] Y. Wang, Y. Xie, H. Sun, J. Xiao, H. Cao, S. Wang, 2D/2D nano-hybrids of gamma-MnO$_2$ on reduced graphene oxide for catalytic ozonation and coupling peroxymonosulfate activation, J. Hazard. Mater. 301 (2016) 56–64.

[45] S. Afzal, X. Quan, S. Lu, Catalytic performance and an insight into the mechanism of CeO$_2$ nanocrystals with different exposed facets in catalytic ozonation of p-nitrophenol, Appl. Catal. B Environ. 248 (2019) 526–537.

[46] Q. Dai, J. Wang, J. Yu, J. Chen, J. Chen, Catalytic ozonation for the degradation of acetylsalicylic acid in aqueous solution by magnetic CeO$_2$ nanometer catalyst particles, Appl. Catal. B Environ. 144 (2014) 686–693.

[47] T. Zhang, W. Li, J.P. Croue, Catalytic ozonation of oxalate with a cerium supported palladium oxide: an efficient degradation not relying on hydroxyl radical oxidation, Environ. Sci. Technol. 45 (2011) 9339–9346.

[48] J. Wang, X. Quan, S. Chen, H. Yu, G. Liu, Enhanced catalytic ozonation by highly dispersed CeO$_2$ on carbon nanotubes for mineralization of organic pollutants, J. Hazard. Mater. 368 (2019) 621–629.

[49] J.Z. Ma, C.X. Wang, H. He, Transition metal doped cryptomelane-type manganese oxidecatalysts for ozone decomposition, Appl. Catal. B-Environ. 201 (2017) 503–510.

[50] S. Zhan, H. Zhang, X. Mi, Y. Zhao, C. Hu, L. Lyu, Efficient Fenton-like process for pollutant removal in electron-rich/poor reaction sites induced by surface oxygen vacancy over cobalt-zinc oxides, Environ. Sci. Technol. 54 (2020) 8333–8343.

[51] Y. Wang, L. Chen, J. Cao, Z. Chi, C. Chen, X. Duan, Y. Xie, F. Qi, W. Song, J. Liu, S. Wang, Role of oxygen vacancies and Mn sites in hierarchical Mn$_2$O$_3$/LaMnO$_{3-\delta}$ perovskite composites for aqueous organic pollutants decontamination, Appl. Catal. B Environ. 245 (2019) 546–554.

[52] Y. Nosaka, A.Y. Nosaka, Generation and detection of reactive oxygen species in photocatalysis, Chem. Rev. 117 (2017) 11302–11336.

[53] H. Zhang, C. Li, L. Lyu, C. Hu, Surface oxygen vacancy inducing peroxymonosulfate activation through electron donation of pollutants over cobalt-zinc ferrite for water purification, Appl. Catal. B Environ. 270 (2020), 118874.

[54] R. Cristina de Oliveira, R.A. Pontes Ribeiro, G.H. Cruvinel, R.A. Ciola Amoresi, M. H. Carvalho, A.J. Aparecido de Oliveira, M. Carvalho de Oliveira, S. Ricardo de Lazaro, L. Fernando da Silva, A.C. Catto, A.Z. Simoes, J.R. Sambrano, E. Longo, Role of surfaces in the magnetic and ozone gas-sensing properties of ZnFe$_2$O$_4$ nanoparticles: theoretical and experimental insights, ACS Appl. Mater. Interfaces 13 (2021) 4605–4617.

[55] J. Xiao, J. Rabeah, J. Yang, Y. Xie, H. Cao, A. Brückner, Fast electron transfer and •OH formation: key features for high activity in visible-light-driven ozonation with C$_3$N$_4$ catalysts, ACS Catal. 7 (2017) 6198–6206.

[56] J. Xiao, Y. Xie, F. Nawaz, S. Jin, F. Duan, M. Li, H. Cao, Super synergy between photocatalysis and ozonation using bulk g-C$_3$N$_4$ as catalyst: a potential sunlight/O$_3$/g-C$_3$N$_4$ method for efficient water decontamination, Appl. Catal. B Environ. 181 (2016) 420–428.

[57] G.F. Yu, Y.X. Wang, H.B. Cao, H. Zhao, Y.B. Xie, Reactive oxygen species and catalytic active sites in heterogeneous catalytic ozonation for water purification, Environ. Sci. Technol. 54 (2020) 5931–5946.

[58] F.Z. Zhang, C.H. Wei, K.Y. Wu, H.T. Zhou, Y. Hu, S. Preis, Mechanistic evaluation of ferrite AFe(2)O(4) (A = Co, Ni, Cu, and Zn) catalytic performance in oxalic acid ozonation, Appl. Catal. A Gen. 547 (2017) 60–68.

[59] Y.X. Huang, Y.R. Sun, Z.H. Xu, M.Y. Luo, C.L. Zhu, L. Li, Removal of aqueous oxalic acid by heterogeneous catalytic ozonation with MnO$_x$/sewage sludge-derived activated carbon as catalysts, Sci. Total Environ. 575 (2017) 50–57.

[60] M. Pedrosa, L.M. Pastrana-Martinez, M.F.R. Pereira, J.L. Faria, J.L. Figueiredo, A. M.T. Silva, N/S-doped graphene derivatives and TiO2 for catalytic ozonation and photocatalysis of water pollutants, Chem. Eng. J. 348 (2018) 888–897.

[61] G. Kresse, J. Hafner, Ab initio molecular-dynamics simulation of the liquid-metal–amorphous-semiconductor transition in germanium, Phys. Rev. B. 49 (1994) 14251–14269.

[62] G. Kresse, J. Furthmüller, Efficient iterative schemes for ab initio total-energy calculations using a plane-wave basis set, Phys. Rev. B. 54 (1996) 11169–11186.

[63] P.E. Blöchl, Projector augmented-wave method, Phys. Rev. B 50 (1994) 17953–17979.

[64] G. Kresse, D. Joubert, From ultrasoft pseudopotentials to the projector augmented-wave method, Phys. Rev. B. 59 (1999) 1758–1775.

[65] W. Hong, M. Shao, T. Zhu, H. Wang, Y. Sun, F. Shen, X. Li, To promote ozone catalytic decomposition by fabricating manganese vacancies in ε-MnO2 catalyst via selective dissolution of Mn-Li precursors, Appl. Catal. B Environ. 274 (2020), 119088.

[66] B. Hammer, L.B. Hansen, J.K. Nørskov, Improved adsorption energetics within density-functional theory using revised Perdew-Burke-Ernzerhof functionals, Phys. Rev. B. 59 (1999) 7413–7421.

[67] H.J. Monkhorst, J.D. Pack, Special points for Brillouin-zone integrations, Phys. Rev. B. 13 (1976) 5188–5192.

[68] Y. Guo, N. Zhang, X. Wang, Q. Qian, S. Zhang, Z. Li, Z. Zou, A facile spray pyrolysis method to prepare Ti-doped ZnFe2O4 for boosting photoelectrochemical water splitting, J. Mater. Chem. A 5 (2017) 7571–7577.

[69] P. Dhiman, N. Dhiman, A. Kumar, G. Sharma, M. Naushad, A.A. Ghfar, Solar active nano-Zn1−xMgxFe2O4 as a magnetically separable sustainable photocatalyst for degradation of sulfadiazine antibiotic, J. Mol. Liq. 294 (2019), 111574.

[70] S.K. Mandal, T.K. Nath, A. Das, Reduction of magnetization in Zn0.9Fe0.1O diluted magnetic semiconducting nanoparticles by doping of Co or Mn ions, J. Appl. Phys. 101 (2007), 123920.

[71] J. Yoon, S. Kim, H. Park, K. Prabakar, O. Lun, Li, Molecular M-N4 macrocycles in a nitrogen-carbon matrix as a highly durable oxygen reduction reaction (ORR) electrocatalysts in acid media, Mater. Lett. 291 (2021), 129561.

[72] X.M. Hu, H.H. Hval, E.T. Bjerglund, K.J. Dalgaard, M.R. Madsen, M.M. Pohl, E. Welter, P. Lamagni, K.B. Buhl, M. Bremholm, M. Beller, S.U. Pedersen, T. Skrydstrup, K. Daasbjerg, Selective CO$_2$ reduction to CO in water using earth-abundant metal and nitrogen-doped carbon electrocatalysts, ACS Catal. 8 (2018) 6255–6264.

[73] J.W. Shi, S.B. Deng, X.Y. Hu, X.J. Sun, S.F. Zhou, L.Y. Fan, W.W. Cai, J. Li, Interconnected porous structural construction of mn- and n-doped carbon nanosheets for fuel cell application, Energy Fuels 36 (2022) 8432–8438.

[74] M.B. Gawande, P. Fornasiero, R. Zbořil, Carbon-based single-atom catalysts for advanced applications, ACS Catal. 10 (2020) 2231–2259.

[75] G.-L. Li, Z.F. Lu, X. Wang, S. Cao, C. Hao, Rational construction of atomically dispersed Mn-Nx embedded in mesoporous N-doped amorphous carbon for efficient oxygen reduction reaction in Zn-Air batteries, ACS Sustain. Chem. Eng. 10 (2021) 224–233.

[76] L. Bai, Z. Duan, X. Wen, R. Si, J. Guan, Atomically dispersed manganese-based catalysts for efficient catalysis of oxygen reduction reaction, Appl. Catal. B-Environ. 257 (2019), 117930.

[77] Y. Wang, N. Ren, J. Xi, Y. Liu, T. Kong, C. Chen, Y. Xie, X. Duan, S. Wang, Mechanistic investigations of the pyridinic N–Co structures in Co embedded N-doped carbon nanotubes for catalytic ozonation, ACS EST Eng. 1 (2021) 32–45.

[78] J. Yang, S. Hu, L. Shi, S. Hoang, W. Yang, Y. Fang, Z. Liang, C. Pan, Y. Zhu, L. Li, J. Wu, J. Hu, Y. Guo, Oxygen vacancies and lewis acid sites synergistically promoted catalytic methane combustion over perovskite oxides, Environ. Sci. Technol. 55 (2021) 9243–9254.

[79] Y. Jia, S. Li, H. Ma, J. Gao, G. Zhu, F. Zhang, J.Y. Park, S. Cha, J.S. Bae, C. Liu, Oxygen vacancy rich Bi$_2$O$_4$-Bi$_4$O$_7$-BiO$_{2-x}$ composites for UV–vis-NIR activated

high efficient photocatalytic degradation of bisphenol A, J. Hazard. Mater. 382 (2020), 121121.

[80] S. Guo, H. Wang, W. Yang, H. Fida, L. You, K. Zhou, Scalable synthesis of Ca-doped α-Fe₂O₃ with abundant oxygen vacancies for enhanced degradation of organic pollutants through peroxymonosulfate activation, Appl. Catal. B Environ. 262 (2020), 118250.

[81] J. Hu, J. Li, J. Cui, W. An, L. Liu, Y. Liang, W. Cui, Surface oxygen vacancies enriched FeOOH/Bi₂MoO₆ photocatalysis-Fenton synergy degradation of organic pollutants, J. Hazard. Mater. 384 (2020), 121399.

[82] Y. Wang, X. Zhang, S. Xi, X. Xiang, Y. Du, P. Chen, D. Lyu, S. Wang, Z.Q. Tian, P. K. Shen, Rational design and synthesis of hierarchical porous Mn–N–C nanoparticles with atomically dispersed MnNx moieties for highly efficient oxygen reduction reaction, ACS Sustain. Chem. Eng. 8 (2020) 9367–9376.

[83] X. Wang, T.-T. Lim, Solvothermal synthesis of C-N codoped TiO₂ and photocatalytic evaluation for bisphenol A degradation using a visible-light irradiated LED photoreactor, Appl. Catal. B Environ. 100 (2010) 355–364.

[84] X. Yu, Z. Bao, J. Barker, Free Radical Reactions Involving Cl•, Cl2-•, and SO4-• in the 248 nm Photolysis of Aqueous Solutions Containing S2O82- and Cl, J. Phys. Chem. A 108 (2004) 295–308.

[85] N. Jaafarzadeh, F. Ghanbari, M. Ahmadi, Efficient degradation of 2,4-dichloro-phenoxyacetic acid by peroxymonosulfate/magnetic copper ferrite nanoparticles/ozone: A novel combination of advanced oxidation processes, Chem. Eng. J. 320 (2017) 436–447.

[86] X. Liu, Z. Yang, W. Zhu, Y. Yang, H. Li, Catalytic ozonation of chloramphenicol with manganese-copper oxides/maghemite in solution: Empirical kinetics model, degradation pathway, catalytic mechanism, and antibacterial activity, Chem. Eng. J. 302 (2022), 114043.

[87] R. Huang, Y. Liu, Z. Chen, D. Pan, Z. Li, M. Wu, C.-H. Shek, C.M.L. Wu, J.K.L. Lai, Fe-species-loaded mesoporous MnO2 superstructural requirements for enhanced catalysis, ACS Appl. Mater. Interfaces 7 (2015) 3949–3959.

[88] Y. Wang, L. Chen, C. Chen, J. Xi, H. Cao, X. Duan, Y. Xie, W. Song, S. Wang, Occurrence of both hydroxyl radical and surface oxidation pathways in N-doped layered nanocarbons for aqueous catalytic ozonation, Appl. Catal. B Environ. 254 (2019) 283–291.

[89] R. Pelalak, R. Alizadeh, E. Ghareshabani, Enhanced heterogeneous catalytic ozonation of pharmaceutical pollutants using a novel nanostructure of iron-based mineral prepared via plasma technology: a comparative study, Appl. Catal. B Environ. 392 (2020), 122269.

[90] F. Wilkinson, W.P. Helman, A.B. Ross, Rate constants for the decay and reactions of the lowest electronically excited singlet state of molecular oxygen in solution. An expanded and revised compilation, J. Phys. Chem. Ref. Data 24 (1995) 663–1021.

[91] D. Bellus, Singlet Oxygen. Reactions with Organic Compounds and Polymers, Wiley, 1978, pp. 1120–1121.

[92] E.T. Yun, J.H. Lee, J. Kim, H.D. Park, J. Lee, Identifying the nonradical mechanism in the peroxymonosulfate activation process: singlet oxygenation versus mediated electron transfer, Environ. Sci. Technol. 52 (2018) 7032–7042.

[93] J. Lee, U. von Gunten, J.H. Kim, Persulfate-based advanced oxidation: critical assessment of opportunities and roadblocks, Environ. Sci. Technol. 54 (2020) 3064–3081.

[94] P. Liang, C. Zhang, X.G. Duan, H.Q. Sun, S.M. Liu, M.O. Tade, S.B. Wang, N-doped graphene from metal-organic frameworks for catalytic oxidation of p-HydroxylbenzoicL acid: N-functionality and mechanism, ACS Sustain. Chem. Eng. 5 (2017) 2693–2701.

[95] L. Qiao, Y. Shi, Q.L. Cheng, B.T. Liu, J. Liu, The removal efficiencies and mechanism of aniline degradation by peroxydisulfate activated with magnetic Fe-Mn oxides composite, J. Water Reuse Desalin. 11 (2021) 212–223.

[96] J. Wang, H. Guo, Y. Liu, W. Li, B. Yang, Peroxymonosulfate activation by porous BiFeO3 for the degradation of bisphenol AF: Non-radical and radical mechanism, Appl. Surf. Sci. 507 (2020), 145097.

[97] L. Yang, Y. Jiao, X.M. Xu, Y.L. Pan, C. Su, X.G. Duan, H.Q. Sun, S.M. Liu, S. B. Wang, Z.P. Shao, Superstructures with atomic-level arranged perovskite and oxide layers for advanced oxidation with an enhanced non-free radical pathway, ACS Sustain. Chem. Eng. 10 (2022) 1899–1909.

[98] F. Guo, K. Wang, J. Lu, J. Chen, X. Dong, D. Xia, A. Zhang, Q. Wang, Activation of peroxymonosulfate by magnetic carbon supported Prussian blue nanocomposite for the degradation of organic contaminants with singlet oxygen and superoxide radicals, Chemosphere 218 (2019) 1071–1081.

[99] Z. Yang, J. Qian, A. Yu, B. Pan, Singlet oxygen mediated iron-based Fenton-like catalysis under nanoconfinement, Proc. Natl. Acad. Sci. USA 116 (2019) 6659–6664.

[100] J. Bing, C. Hu, Y. Nie, M. Yang, J. Qu, Mechanism of catalytic ozonation in Fe2O3/Al2O3@SBA-15 aqueous suspension for destruction of ibuprofen, Environ. Sci. Technol. 49 (2015) 1690–1697.

[101] S.S. Sable, P.P. Ghute, D. Fakhrnasova, R.B. Mane, C.V. Rode, F. Medina, S. Contreras, Catalytic ozonation of clofibric acid over copper-based catalysts: In situ ATR-IR studies, Appl. Catal. B Environ. 209 (2017) 523–529.

[102] S. Li, J. Huang, Z. Ye, Y. Wang, X. Li, J. Wang, L. Li, The mechanism of Metal-H2O2 complex immobilized on MCM-48 and enhanced electron transfer for effective peroxone ozonation of sulfamethazine, Appl. Catal. B Environ. 280 (2021), 119453.

[103] T. Zhang, W. Li, J.-P. Croué, Catalytic ozonation of oxalate with a cerium supported palladium oxide: an efficient degradation not relying on hydroxyl radical oxidation, Environ. Sci. Technol. 45 (2011) 9339–9346.

[104] C. Rajani, J.R. Kincaid, D.H. Petering, Resonance Raman studies of HOO−Co(III) bleomycin and Co(III) bleomycin: identification of two important vibrational modes, ν(Co−OOH) and ν(O−OH), J. Am. Chem. Soc. 126 (2004) 3829–3836.

[105] I.G. Denisov, P.J. Mak, T.M. Makris, S.G. Sligar, J.R. Kincaid, Resonance Raman characterization of the peroxo and hydroperoxo intermediates in cytochrome P450, J. Phys. Chem. A 112 (2008) 13172–13179.